



Investigating electrode calendering and its impact on electrochemical performance by means of a new discrete element method model: Towards a digital twin of Li-Ion battery manufacturing

Alain C. Ngandjong ^{a,b,1}, Teo Lombardo ^{a,b,1}, Emiliano N. Primo ^{a,b}, Mehdi Chouchane ^{a,b}, Abbas Shodiev ^{a,b}, Oier Arcelus ^{a,b}, Alejandro A. Franco ^{a,b,c,d,*}

^a Laboratoire de Réactivité et Chimie des Solides (LRCS), UMR CNRS 7314, Université de Picardie Jules Verne, Hub de l'Energie, 15, rue Baudelocque, 80039, Amiens Cedex, France

^b Réseau sur le Stockage Electrochimique de l'Energie (RS2E), FR CNRS 3459, Hub de l'Energie, 15, rue Baudelocque, 80039, Amiens Cedex, France

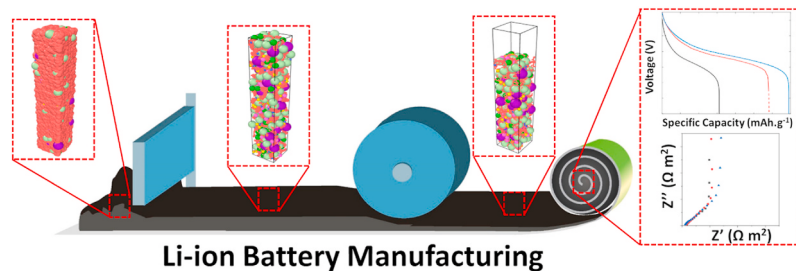
^c ALISTORE-European Research Institute, FR CNRS 3104, Hub de l'Energie, 15, rue Baudelocque, 80039, Amiens Cedex, France

^d Institut Universitaire de France, 103 Boulevard Saint Michel, 75005, Paris, France

HIGHLIGHTS

- Experimentally validated Discrete Element Method calendering model.
- Explicit consideration of Active Material and Carbon-Binder domain phases.
- Effect of calendering on mesoscale electrode properties of NMC-based cathodes.
- Effect of mesoscale electrode properties on macroscale electrochemical observables.
- Towards a digital twin of the full LIBs manufacturing process.

GRAPHICAL ABSTRACT



ARTICLE INFO

Keywords:

Lithium-ion batteries
Manufacturing
Digital twin
Calendering
Discrete element method
Electrode mesostructure

ABSTRACT

Lithium-ion battery (LIB) manufacturing optimization is crucial to reduce its CO₂ fingerprint and cost, while improving their electrochemical performance. In this article, we present an experimentally validated calendering Discrete Element Method model for LiNi_{0.33}Mn_{0.33}Co_{0.33}O₂-based cathodes by considering explicitly both active material (AM) and carbon-binder domain (CBD). This model was coupled to a pre-existing Coarse-Grained Molecular Dynamics model describing the slurry equilibration and its drying and a 4D-resolved Finite Element Method model for predicting electrochemical performance. Our calendering model introduces important novelties versus the state of the art, such as the utilization of un-calendered electrode mesostructures resulting from validated simulations of the slurry and drying combined with the explicit consideration of the spatial distribution and interactions between AM and CBD particles, and its validation with both experimental micro-indentation and porosity vs. calendering pressure curves. The effect of calendering on the electrode mesostructure is analyzed in terms of pore size distribution, tortuosity factor and particles arrangement. In addition, the evolution of the macroscopic electrochemical behavior of the electrodes upon the degree of calendering is discussed, offering

* Corresponding author. Laboratoire de Réactivité et Chimie des Solides (LRCS), UMR CNRS 7314, Université de Picardie Jules Verne, Hub de l'Energie, 15, rue Baudelocque, 80039, Amiens Cedex, France.

E-mail addresses: alejandro.franco@u-picardie.fr, alejandro.franco@u-picardie.fr (A.A. Franco).

¹ These authors have equally contributed to this article.

added insights into the links between the calendering pressure, the electrode mesostructure and its overall performance.

1. Introduction

The evolution of modern society calls for flexible, economically and ecologically sustainable energy storage technologies able to meet the needs of both individuals and the market. Li-ion batteries (LIBs) are, undoubtedly, one of the technologies which play a predominant role in transportation [1], portable electronics [2] and renewable resources [3]. Several strategies can be attempted to improve their performance, by reducing in the meantime their costs and manufacturing CO₂ fingerprint [4–7]: among them, the better understanding and control of LIB cells manufacturing [8–10]. Complementary to the experimental approach [11–16], the use of mesoscale modeling to investigate the effect of manufacturing parameters on the electrode mesostructure and electrochemical performance starts to be recognized as significantly important [17–27]. In order to improve the reliability of the modeling results, the explicit consideration of the electronic conductive carbon additive and binder phase, together with the active material (AM), has been recently demonstrated to be critical [20–22,28,29]. From the experimental point of view, the imaging techniques available today do not allow to easily resolve the carbon location, due to its low atomic mass and X-ray cross section, compared to the ones of the most common cathode AMs [30–32]. So far, only few experimental works have achieved that, such as the one reported by Lu *et al.* [26] who implemented a dual-scan superimposition technique using X-ray nano-CT to discriminate between AM, carbon-binder domain (CBD) and pore phases.

In this sense, experimentally validated mesoscale models aiming at simulating LIB manufacturing can precisely track the position of both AM and CBD along the fabrication process chain and analyze its effect in terms of electrochemical performance, as clearly demonstrated by us in a series of previous works [18,20–24]. Among these steps, calendering has been widely recognized to strongly impact the final electrode characteristics both experimentally [33–38] and computationally [39–43]. Calendering can be defined as the compression of the dried electrode (the latter resulting from the coating and drying of an electrode slurry) in order to reduce its porosity, improve the particles contacts and enhance its energy or power density. Nonetheless, the electrode compression is also detrimental for other critical electrode properties, such as the effective conductivity of the electrolyte phase [44]. From the computational point of view, different approaches to model this process have been proposed [19,39–42]. Stershic *et al.* reported a fabric tensor-based approach to capture the inter-particles connectivity, which was linked to the structural and transport properties of the electrode, and a discrete element method (DEM) simulation to model the calendering [42]. This study was performed by using as starting point (*i.e.* the un-calendered electrode) a tomography image not considering the CBD phase, which is expected to significantly influence the obtained results. Giménez *et al.* published a series of works [39–41] in which they propose a DEM model able to capture the mechanics of LiNi_xMn_yCo_{1-x-y}O₂ (NMC)-based electrodes through the comparison between experimental and simulated nano-indentation curves. Even if these results are surely of interest to better understand the mechanics of NMC-based cathodes, the electrode structure before the calendering was generated stochastically and considers only AM particles. The presence of binder was modelled by generating bonds between AM particles, which could break if they undergo a force over a certain threshold value. Such approach has two main disadvantages: (*i*) the trustability of the stochastically generated electrode, which most likely affects all the results obtained in these studies and that does not allow linking this structure to any manufacturing condition in terms of slurry properties and drying; (*ii*) it does not allow to track the position of carbon aggregates, which, as discussed above, was demonstrated to have a critical

impact on the electrochemistry [21,22]. Srivastava *et al.* [19] proposed a DEM-based approach to simulate the effect of cohesive and adhesive forces on the electrode mesostructure properties as the particles aggregation and tortuosity. In their approach, an initial structure containing AM and CBD particles is stochastically generated. Then, the drying and calendering are modelled by compressing the simulation box up to the desired dimensions and by letting the force fields (FFs) acting between the AM and CBD particles to equilibrate the system. The difference between drying and calendering in their approach relies on turning on/off the Brownian motion of the CBD particles, respectively. Although their studies in terms of adhesive and cohesive effects are innovative, this approach lacks in describing the slurry properties explicitly and it is not validated through experimental results, which should be performed to enhance the reliability of the so-obtained electrode mesostructures.

In our previous publications, we have reported a digital twin allowing to simulate in an experimentally-validated and consistent way electrode slurries and their drying, by considering the AM particles and the CBD as separated phases. In addition, we have already explored the electrochemical performance of the resulting (un-calendered) electrodes by means of continuum models solved using the Finite Element Method (FEM) [18,21–24]. Our previously reported approach simulates the slurry equilibration and drying by using Coarse Grained Molecular Dynamics (CGMD), in which the CBD in the slurry contains also the solvent. The drying simulation consists in shrinking the CBD particles to remove the solvent, by changing accordingly the FFs parameters values. This approach relies on Lennard-Jones and Granular-Hertzian FFs for both the slurry and the drying, similarly to the previous work reported by Forouzan *et al.* [27]. In our previous publications we carried out a deep parametrization and validation of the CGMD FFs to accurately simulate the slurry phase with different compositions and solid contents [18] by comparing systematically experimental and simulated observables (shear-viscosity curve and slurry density). In addition, this computational framework was further extended by implementing 4D-resolved (space and time) FEM models [20–22] for simulating the cell galvanostatic discharge and electrochemical impedance spectroscopy (EIS) characterizations of the predicted electrode mesostructures.

In the present work, we report a step further into the development of our LIB manufacturing digital twin by implementing a novel DEM calendering model within our computational framework. The model, its validation (by comparing simulated and experimental results) and the effect of calendering on mesostructural and macroscale electrochemical properties (and their interdependencies) are the core of this work. Compared to the state of the art, the novelty introduced here is to report an experimentally validated 3D calendering model that (*i*) explicitly considers the CBD particles, (*ii*) is embedded in a 3D LIBs manufacturing digital twin in which both slurry and dried electrode phases were explicitly considered and experimentally validated and (*iii*) can be injected into a 4D continuum model, assigning different physics to AM and CBD particles, to assess the resulting electrodes electrochemical properties.

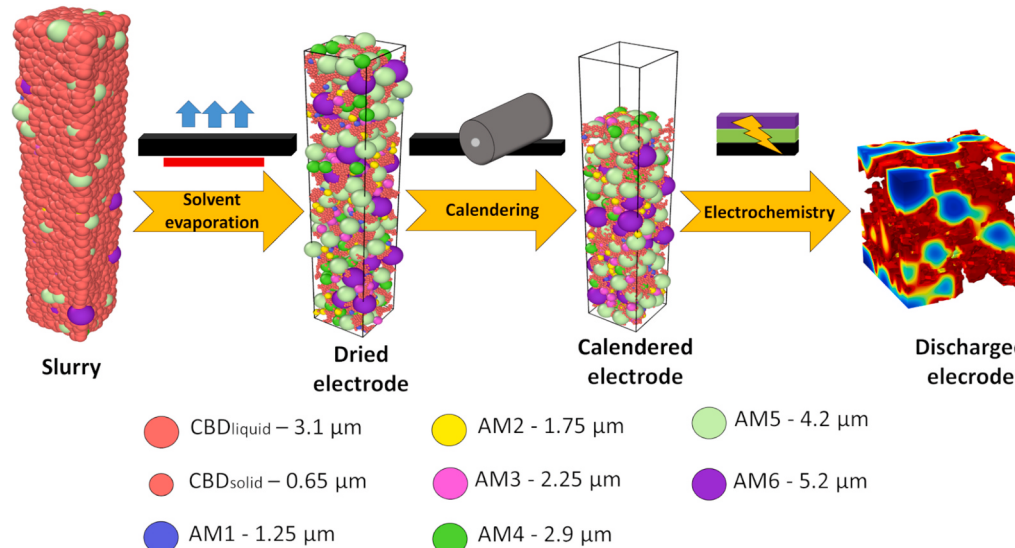
2. Model workflow and validation

The computational workflow of our methodology is schematized in Fig. 1. First, the slurry phase is simulated through CGMD by using as input the experimental composition and AM particle size distribution. The electrode composition analyzed in this work consisted in 96 wt% LiNi_{0.33}Mn_{0.33}Co_{0.33}O₂ (NMC, Umicore), 2 wt% carbon black (C-NERGY™ super C65, Imerys) as conductive additive and 2 wt% Polyvinylidene fluoride (PVdF, Solef™ 5130/1000, Solvay) as binder. The experimental AM particle size distribution (obtained through Scanning

Electron Microscopy images) is reported in the Supporting Information, section S1. N-methylpyrrolidone (NMP, BASF) was used as solvent and the slurry solid content (SC) was 69 wt%. From the computational point of view, the number of CBD particles needed to match the experimental electrode composition was calculated by using a CBD density of 0.95 g cm^{-3} instead of the experimental one (1.81 g cm^{-3}), similarly to Srivastava *et al.* [19]. This corresponds to CBD particles with a nanoporosity equal to $\sim 47\%$, as previously measured through high-resolution FIB-SEM images [45]. The radius of each particle type is reported in the legend of Fig. 1.

As discussed in our previous publications [18,24], the CGMD approach considers two kinds of particles: AM and CBD. At the slurry stage, the solvent is taken into account by decreasing the CBD density and increasing its diameter. The FFs used in the CGMD simulations to describe the interactions between the particles are the Lennard-Jones [46] (LJ) and the Granular Hertzian [47] (GH). The GH describes the mechanical properties of the system, while the LJ mimics the adhesive forces between particles. For the interested readers, a detailed discussion around these FFs can be found in Refs. [18,46,47]. The slurry phase is then validated by comparing the experimental and simulated slurry density (ρ) and shear-viscosity ($\eta \cdot \dot{\gamma}$) curves, as discussed extensively in our previous publication [18]. The slurry validation for the case study reported in this work is summarized in Fig. S2, in the Supporting Information.

The dried electrode mesostructure is obtained using as input the experimentally validated simulated slurry. First, the CBD particles (containing also the solvent in the slurry phase) are shrunk from a radius of $3.1 \mu\text{m}$ down to $0.65 \mu\text{m}$, in order to mimic the solvent removal. Afterwards, a second CGMD simulation is performed to obtain the equilibrated dried electrode mesostructure. This second CGMD simulation was carried out by using the same FFs (LJ + GH). However, the FFs parameters were changed accordingly to match the transformation from a viscous liquid-like system (slurry) to a solid one (electrode). For instance, the stiffness of the system is expected to increase after the solvent evaporation, so the elastic constant (within the GH FF term) and the potential well (within the LJ FF term) were increased. The exact value of the FFs parameters are then modulated to match the experimental electrode density and porosity, as summarized in Table 1. The list of the CGMD FFs parameter values used for the slurry and dried electrode simulations are reported in Tables S1 and S2 in the Supporting information.

**Table 1**

Comparison of experimental (with associated standard deviation) and simulated density and porosity of the dried electrode.

| | $\rho (\text{g cm}^{-3})$ | Porosity (%) |
|--------------|---------------------------|--------------|
| Experimental | 2.3 ± 0.1 | 42 ± 2 |
| Simulated | 2.4 | 41.6 |

The dried electrode mesostructure is then embedded in a DEM model which simulates its mechanical behaviour along the calendering process. The boundary conditions used for the DEM simulation were considered as periodic only in the x and y directions (Fig. 1). The FFs used were the GH [48] and the simplified Johnson-Kendall-Roberts [49, 50] (SJKR). As for the case of the CGMD simulations, GH (Eq. (1)) represents the mechanical properties of the system, while SJKR (Eq. (2)) corresponds to the adhesive forces, principally due to the binder “bridges”.

$$F_{GH} = \sqrt{\delta} \sqrt{\frac{R_i R_j}{R_i + R_j}} [(k_n \delta n_{ij} - m_{eff} \gamma_n v_n) - (k_t \Delta s_t + m_{eff} \gamma_t v_t)] \quad (1)$$

$$F_{SJCR} = CED \times A \quad (2)$$

In Eq. (1), k_n , k_t , γ_n and γ_t symbolize the normal and tangential elastic and viscoelastic damping constant; while v_n and v_t stand for the relative normal and tangential velocity components between two interacting bodies, respectively. Δs_t , m_{eff} and n_{ij} represent the tangential displacement vector, the effective mass $\left(\frac{m_i m_j}{m_i + m_j}\right)$ and the unit vector along the line connecting the centre of the two interacting bodies. $R_{i,j}$ and δ are the particles radii and the overlap distance, respectively. It should be noted that a certain degree of overlap is needed for GH to be non-zero, here considered by slightly expanding (2%) the AM particles diameter. All the GH parameters discussed above are linked to the macroscopic properties of the modelled materials. Specifically, the elastic constant is associated to the Young modulus (E), while the damping factor, to the coefficient of restitution (e). Moreover, the ratio between the normal and tangential elastic constants and damping factors depends on the Poisson ratio (ν), while the coefficient of friction (X_u) defines the maximal ratio between the normal and tangential GH forces [48,51]. On the other hand, the SJKR is related to the cohesion energy density (CED) and the contact

force (A) between the two interacting bodies.

Fig. 1. Computational workflow adopted in this work. First, the slurry phase (left) is simulated through CGMD using as input the experimental composition and AM particle size distribution. Afterwards, the dried electrode (middle left) is obtained by performing another CGMD simulation, using as input the slurry mesostructure, whose CBD particles (containing also the solvent at the slurry phase) are shrunk in order to mimic the solvent evaporation. The calendering (middle right) is simulated through a DEM model by applying a pressure through a moving plane initially placed in the upper limit of the simulation box. Lastly, the electrochemical performance (right) is assessed through continuum (FEM) models. The legend at the bottom reports the colour and the radius associated to all the particle types considered along the manufacturing simulations. (For interpretation of the references to colour in this figure legend, the reader is referred to the Web version of this article.)

area between two interacting bodies (A). Therefore, the CED represents a proportionality constant related to the adhesive force strength per unit of contact surface. F_{SJCR} is computed whenever two bodies are in contact, acting as a force which opposes the detachment of the two interacting bodies. If a force higher than F_{SJCR} is developed due to the calendering, the two particles are separated, as it happens when a binder bridge is broken. However, if two particles come into contact again, the F_{SJCR} is computed, which can be considered as the re-forming of the binder bridges. Two planes were added at the top and bottom of the simulation box to model the calender rolls and the current collector, respectively. The planes E were selected to match the ones previously reported [42, 52] for stainless steel (calender rolls) and aluminum (current collector). The NMC particles E reported in literature ranges between 100 and 200 GPa [42, 53–55], choosing the upper limit for our simulations. All the other parameters (Table 2) were modulated to match the experimental mechanical properties of the dried electrode and its behaviour along the calendering process. For that purpose, the electrode micro-indentation curve was obtained through the DEM simulations and then compared to the experimental one using the same electrode composition.

Micro-indentation uses a point indenter to deform a material on a micro-scale and this deformation is directly related to its hardness and E. This method typically uses an indenter that penetrates the surface of the specimen upon application of a given load at a constant rate, and registers its displacement during the load and unload [56]. Due to its direct correlation with the mechanical properties of the sample, the experimental load-displacement curve of the electrode was used to parametrize the calendering model, by fitting this curve with a simulated one over the modelled electrode. Both in experimental and modeling, the electrode was compressed up to 10% of its initial thickness, which afterwards is pulled back to its original position. Even if the experimental and simulated electrode thickness ($\sim 180 \mu\text{m}$ and $\sim 154 \mu\text{m}$, respectively) are comparable, it is computationally too costly to simulate the compression of a surface as large as the experimental one ($\sim 31000 \mu\text{m}^2$). Considering that the contact surface between the indenter and the electrode has a direct impact on the measured force, both the force and the indenter/plane displacements were normalized relative to the maximal force/displacement obtained both experimentally and computationally. This allows a consistent comparison of the experimental and modeling results (Fig. 2A). Furthermore, the electrode surface area can have an impact on the micro-indentation curve shape. Consequently, several tests were performed to find the minimal electrode surface area for which no size effect was observed, as discussed in the Supporting Information, Section S3.

In order to further validate the DEM model and the associated FFs parametrization, the modelled and experimental electrode porosity profile in terms of the calendering pressure were compared, as reported in Fig. 2B. It is important to highlight that the same FFs parameters (Table 2) were used for both micro-indentation curve and calendering simulation. The calendering (similar to the indentation measurements) is performed in two steps. First, the upper plane is moved down until reaching a certain value of pressure. Afterwards, the plane is moved up to the initial position, which leads to a relaxation of the electrode

mesostructure. The latter is done in order to consider the elastic recovery of the structure following the compression, as previously reported [41]. Therefore, in order to correctly compare the experimental and simulated curves, the pressure reported in Fig. 2B refers to the pressure applied at the end of the compression, while the porosity is the one calculated after the electrode elastic recovery. Overall, Fig. 2 demonstrates the validity of the model herein proposed in terms of capturing both the electrode mechanics and the porosity evolution along the calendering. To the best of our knowledge, this is the first time that such validation, considering simultaneously two different descriptors, is performed for a DEM electrode calendering model which accounts explicitly for the AM and CBD phases.

Table 2 shows that CBD particles CED is smaller than the one of the other materials, even though the opposite trend was expected at first. However, during the parametrization it was noticed that higher values of CED should be, at least, partially counter-balanced by higher values of E. Otherwise, particle overlap would become predominant, which has no physical ground. The above shows how the mechanical properties of the system arise from a complex interplay of the forces acting on it (GH and SJCR in the model proposed here).

3. Structural characterization

Calendering is typically performed to decrease the electrode porosity in order to maximize the particles contacts and increase its energy or power density and it is known to affect the electrode mesostructure, which in turns strongly influences the electrochemical performance. Therefore, in this section we study its impact in terms of properties that are accessible experimentally (such as the pore size distribution (PSD) or the tortuosity factor), but are difficult to obtain routinely or affected by several approximations [21], and properties that cannot be obtained through experiments, such as the particles radial distribution function.

As expected, the electrode compression does not only influence the average porosity (as seen in Fig. 2B), but also the PSD. Fig. 3 reports the experimental and simulated PSD, measured through Hg intrusion porosimetry and by the open-source software PorosityPlus [57, 58] (adapted to our case study), respectively.

As expected, both the overall amount of pores and their size decrease by reducing the porosity (i.e. by increasing the calendering pressure). However, the pore radii found through Hg intrusion and PorosityPlus are significantly different. The latter is due to the differences and the approximations behind both methodologies. Hg intrusion porosimetry is based on applying an external pressure in order to force the liquid Hg into the porous structure. Being Hg a not wetting liquid for the majority of materials (contact angle $> 90^\circ$), the pressure needed to fill the pores is proportional to the pore cross-sectional area [59]. Particularly, the smaller the pore, the higher the pressure that should be applied. Consequently, the pressure applied can be used to calculate the pores dimension through the Washburn equation [60]. However, the latter assumes a cylindrical pore shape. On the other hand, PorosityPlus calculates the PSD by trying to fit as much as possible spheres into the electrode pores. Consequently, the x axis of Fig. 3A and B then refer to different radii (cylinder and sphere radius, respectively). Lastly, the use of a coarse-grained approach (CGMD and DEM) is expected to influence the PSD, considering the lack of explicit CBPs inner-porosity and the fact that this particle represents an agglomerate of carbon black and binder. In spite of the above, the overall trend (pore amount and size decreasing by increasing the calendering pressure) is further confirmed by using the PSD algorithm firstly developed by Dong et al. [61] and subsequently modified by Torayev et al. [62] considering both spherical and cylindrical pores, as reported in section S4 of the Supporting Information.

The radial distribution function $g(r)$ measures the particles local arrangement of a phase i (either AM or CBD) around a certain particle type j , normalized by the average particle density in the overall simulated electrode. The latter allows to identify if there is a certain degree of order (identifiable as a peak in the $g(r)$ curve) or not, therefore offering

Table 2

DEM parameters used for both micro-indentation and calendering. The mixed interactions i-j (ex. AM-CBD) for e, v and Xu correspond to the geometric mean of each property associated to the materials i and j. The AM and CBD dimensions and density were kept constant relative the ones used for the dried electrode CGMD simulation (Table S2).

| | AM | CBD | Al | Steel |
|--|-----------------|-----------------|-------------------|-----------------|
| E [GPa] | 200 | 2 | 69 | 200 |
| E | 0.15 | 0.15 | 0.5 | 0.78 |
| v | 0.3 | 0.5 | 0.3 | 0.3 |
| Xu | 0.001 | 0.001 | 1.2 | 0.76 |
| CED ($\text{pg } \mu\text{m}^{-1} \mu\text{s}^{-2}$) | 6×10^5 | 7×10^4 | 5.5×10^5 | 6×10^5 |

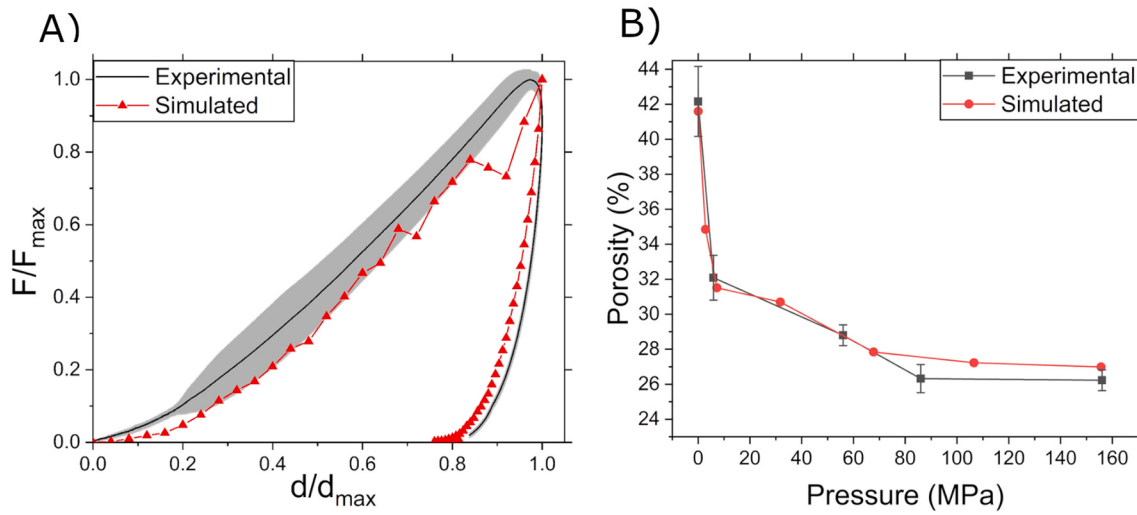


Fig. 2. Mechanical model validation. A) Comparison of experimental (black line) and simulated (red line/dots) microindentation curve. The experimental curve corresponds to an average of 30 independent measurements, the grey area represents the standard deviation. The experimental and simulated electrode maximal contact surface and displacement are equal to $\sim 31000 \mu\text{m}^2/\sim 18 \mu\text{m}$ and $\sim 11600 \mu\text{m}^2/\sim 16 \mu\text{m}$, respectively. B) Comparison of experimental (black) and simulated (red) evolution of the electrode porosity as a function of the applied calendering pressure. The error bars represent the experimental standard deviation. (For interpretation of the references to colour in this figure legend, the reader is referred to the Web version of this article.)

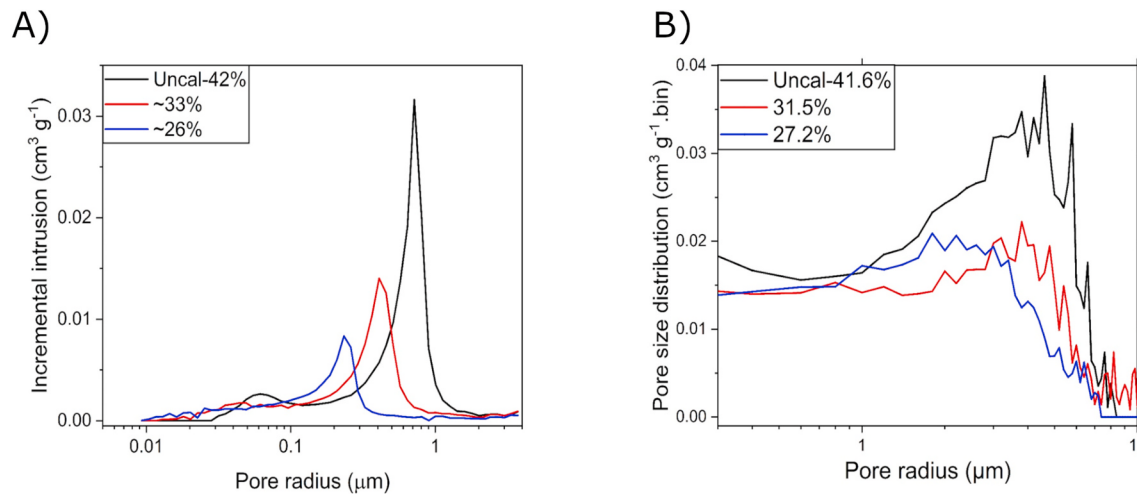


Fig. 3. A) Experimental PSD obtained through Hg intrusion porosimetry and normalized by the electrode mass. B) Pore size distribution of the simulated electrode (normalized by its mass, while the bin indicates the resolution used for the calculation) calculated by the open source software PorosityPlus [57], which was adapted to our case study.

information about the short/long range particles arrangement in the electrode mesostructure.

Fig. 4A reports the $g(r)$ as a function of the distance between CBD particles, showing that CBD particles tend to aggregate for both uncalendered and calendered electrodes. Particularly, two main ordered zones can be identified at distances $\sim 1.25 \mu\text{m}$ (first shell) and $\sim 2 \mu\text{m}$ (second shell), respectively. After the calendering, both the first peak width at half the maximum and the height of all the peaks associated to the second shell decrease. The latter indicates that upon calendering CBD aggregates are compacted, thus enhancing the CBD organization of the first shell, while the ordering at longer distances is lost. Moreover, by reducing the electrode porosity due to calendering (red vs. blue curve), the tail of the peak at $\sim 1.25 \mu\text{m}$ increases at the expense of its height, implying that a small fraction of CBD particles move even closer to each other. The local order of CBD around AM (Fig. 4B) is significantly increased when calendering. Notably, the calendered structures display six main peaks, whose x coordinates are slightly higher than the radii of the six AM particle types considered in our simulations (Fig. 1). The

latter clearly indicates that upon calendering CBD particles cover each AM particle type filling the AM-AM interstitial pores. Moreover, by increasing the applied calender pressure (red vs. blue curve) the peaks distances do not change. This demonstrates that calendering decreases the AM-CBD particles distances up to a certain limit. As in the case of AM-CBD, the AM-AM $g(r)$, reported in Fig. 4C, shows that calendering induces a locally ordered structure in terms of AM particles location. Moreover, the x coordinates of the calendered structures principal peaks are slightly higher than the sum of two AM particle radii (Fig. 1), which would suggest that each peak is associated to a certain arrangement of two AM particle types in the space, as discussed in more detail in the Supporting Information, Section S5.

The impact of calendering on the electrolyte effective properties within the porous electrode can be captured by its tortuosity factor [63]. The tortuosity factors here reported were calculated by solving the first Fick's law and applying the MacMullin equation [64] through GeoDict [65] computational software for each Cartesian direction (x , y , z). Moreover, the Bruggeman corrected effective diffusivity ($D_{\text{eff}} =$

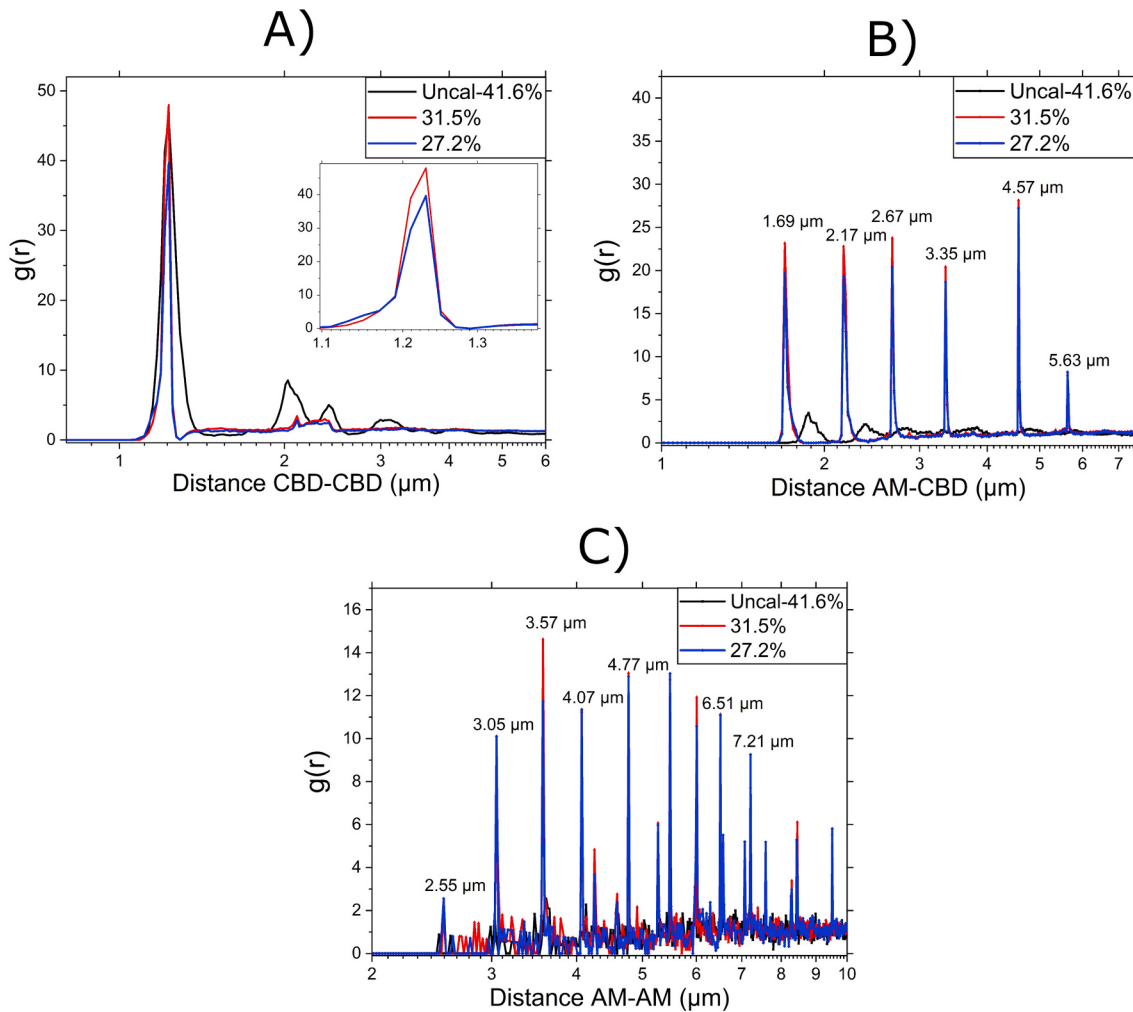


Fig. 4. Radial distribution function $g(r)$ of the un-calendered electrode (black curve) and electrodes calendered up to 31.5% (red curve) and to 27.2% (blue curve) porosity for A) CBD-CBD, B) CBD-AM and C) AM-AM particles. The distances were calculated from the center of mass of A) CBD, B) AM and C) AM particles. The inset in Fig. 4A displays a zoom of the first peak for the two calendered structures to ease their comparison. (For interpretation of the references to colour in this figure legend, the reader is referred to the Web version of this article.)

$D_{\text{bulk}} * \varepsilon^{1.5}$, where D_{bulk} is the bulk electrolyte diffusivity and ε , the porosity) was assigned to the CBD phase in order to consider an inner-porosity of 47%. The evolution of the tortuosity factor τ [66] as a function of the applied pressure is reported in Fig. 5.

The results show that τ increases by increasing the calendering pressure, reaching a plateau-like behavior for high pressures. Interestingly, the evolution of τ upon calendering is similar for all the Cartesian directions, indicating that calendering influences the transport properties of the electrolyte over the whole electrode mesostructure and not only along the direction of compression.

4. Electrochemical characterization & performance

This section deals with the electrochemical properties evolution upon calendering and its correlation to the mesostructure features analyzed previously. The simulations were performed in COMSOL Multiphysics® environment, which relies on FEM. The electrode mesostructures resulting from the CGMD followed by the DEM simulations were imported into COMSOL using our INNOV algorithm in order to generate the meshes [67]. An *in silico* symmetric cell was generated in order to perform EIS simulations. Previously, we showed that our 4D-resolved model [21] can be used to capture the changes of electronic and ionic resistances. The symmetric cell was constructed by duplicating the meshed electrode mesostructures, separated by a 12 μm thick

Celgard separator based on the SEM images from the open-source data of Lagadec *et al.* [68]. A 5 μm thick current collector was added to the extremes of the *in silico* cell.

The obtained Nyquist plots for the un-calendered and calendered electrodes are displayed in Fig. 6A. The EIS response can be roughly divided into three different regions: high frequency ($>10^5$ Hz), sloping mid-frequency ($1\text{--}10^5$ Hz) and horizontal straight low frequency ($<1\text{Hz}$). The high-frequency intercept into the real axis is generally associated with the electrode electronic resistance and the resistance of the separator, the sloping mid-frequency region with electrolyte ionic resistance within the porous electrode, and the low-frequency one corresponds to the double layer formation [21,69,70]. Fig. 6A shows that by increasing the applied calender pressure the high frequency intercept shifts to lower values, indicating lower electronic resistance of the solid phase [21]. This trend perfectly matches the ones previously discussed in terms of particle distances (Fig. 4). Additionally, the low-frequency region shows an ideal 90° behavior because the CBD/electrolyte interface was treated in the model as ideally polarizable, with constant double-layer capacitance. The length of the mid-frequency sloping region increases by increasing the calendering pressure, indicating a rise of the effective electrolyte ionic resistance upon calendering [21,69,71]. The latter is directly linked to the decrease in the electrode porosity (Fig. 2B) and pores size distribution (Fig. 3B), which slows down the migration and diffusion rate of ions within pores [21]. Moreover, the

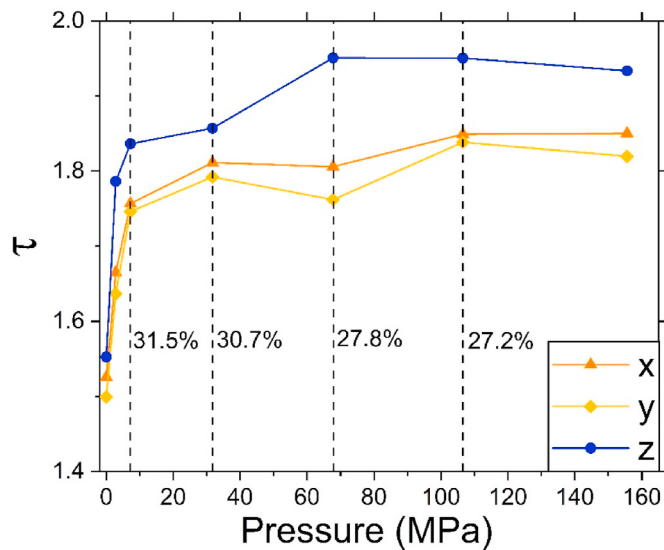


Fig. 5. Tortuosity factor for calendered and not calendered electrodes as a function of the applied calendering pressure for x , y and z Cartesian directions by considering a CBD inner porosity of 47%. The dashed lines and the associated values correspond to the electrode macroporosity (Fig. 2B) for the applied calendering pressures.

length of this region is directly linked to the EIS tortuosity factor (τ_{EIS}), whose calculated values (Table 3) are in agreement with the ones obtained through GeoDict diffusivity methodology (Fig. 5). Fig. 6B displays the ionic contribution to the overall impedance of a cross-sectional cut at half the electrode thickness at 100 Hz. Within our models formality, CBD has 47% of inner porosity treated as a region permeable to the electrolyte diffusion. The effective ionic diffusion coefficient is corrected through a Bruggeman relation. Therefore, in the 2D plots of Fig. 6B, the ionic contribution comes from the electrolyte within the pores and the accessible region within the CBD phase. In this sense, as the contact between the CBD particles increases and the porosity decreases upon calendering, the ionic contribution to the total impedance grows.

We simulated a single discharge at a rate equal to 1C (NMC specific capacity = 280 mAh g⁻¹) to probe the impact of the calendering process on the electrochemical performance. Fig. 7A depicts the 3D meshed renders for each calendering conditions (more information can be found in the Computational Methods section). The un-calendered electrode displays a specific capacity of 116.2 mAh g⁻¹ (black curve in Fig. 7B), lower than both the calendered electrodes (121.5 and 130.7 mAh g⁻¹, respectively). Fig. S8 (Supporting Information) reports the experimental results of discharge curves at 1C for different calendering pressures, displaying the same trend in terms of calendered electrodes. Experimentally, an un-calendered electrode with low mass ratio of the conductive phase (96:2:2, NMC:CB:PVDF) shows virtually no capacity at high C-rate due to its low electronic conductivity. The same result would be expected computationally if further decreasing the AM electronic conductivity, which is currently not possible due to numerical limitations in Comsol Multiphysics®. In Fig. 7B, the simulated specific capacity of the un-calendered electrode is lower than the calendered ones, but the discharge voltage is higher in the first half of the curve, until it drops sharply around 70 mAh.g⁻¹. The opposite trend in terms of potential would have been expected, due to the ohmic drop caused by the poor electronic conductivity of the un-calendered electrode. This opposite behavior can be explained by the changes in the contact surface between the particles and the current collector. Indeed, this contact surface is higher for the un-calendered electrode than the calendered ones, while the opposite trend is expected. Therefore, for a given C-rate the current density at the current collector plane is lower for the un-

calendered electrode, leading to a smaller ohmic drop during the first half of the discharge. However, the poor electronic transport of the un-calendered electrode leads to a rapid drop of the potential in the second half. The trend in the contact surface between particles and the current collector is due to the different periodic boundary conditions used in the CGMD model for the drying (all boundaries considered as periodic) and in the DEM model for the calendering (z boundary considered as not periodic). This calls for an improve model of drying with non-periodic boundary condition along z , which is currently under development in our group. Despite this limitation of the drying model used, the above demonstrates the capability of our multiscale approach (sequential coupling between CGMD, DEM and FEM) to capture the calendering effect on the electrochemical properties. The experimental capacities being systematically lower than the simulated ones is due to the different theoretical capacities and AM electronic conductivity in the simulation vs. the experimental one, which were increased in this model in order to ensure a fast simulation convergence.

The strength of this methodology is to investigate at the mesoscale the relation between manufacturing process and performance. Fig. 7B highlights that polarization decreases upon calendering for the case of the calendered electrodes. Polarization can have different origins, as poor electronic conductivity due to a limiting percolation network or limited ionic transport due to low porosity or high tortuosity factor. As it was shown in Fig. 4 A and B, the average distances between CBD-CBD and AM-CBD particles slightly decrease by increasing the calendering pressure. Therefore, it would be expected to obtain a more extended percolating network for the 27.2% porous electrode. To better understand the CBD network interconnectivity, we analyzed the current density going through this phase. Its homogeneity is crucial for providing a good electronic conductivity and to avoid local overpotential hot spots. A wide local current density dispersion would hinder the performance, since it would mean a heterogeneous current density distribution. To quantify this contribution, the CBD transport observable reported in Fig. 7C is defined as the inverse of the average standard deviation of the local current density going through the CBD. This property is significantly enhanced through calendering (by a factor of ~3 when comparing the un-calendered electrode vs. the less porous one). Furthermore, the tortuosity factor increases by increasing the calendering pressure (Fig. 5), which leads to a decrease in the efficiency of Li⁺ transport. For quantifying the latter, an electrolyte transport observable was defined as the inverse of the average Li⁺ concentration gradient along the z axis at 110 mAh.g⁻¹: the higher its value, the lower the limitation in Li⁺ flux. The un-calendered electrode displays the highest value since it has the lowest tortuosity factor and highest porosity. Upon calendering, the electrolyte transport observable decreases, as the tortuosity factor and porosity increases and decreases, respectively. Lastly, the lower porosity and distances between solid particles (Figs. 2 and 4, respectively) impact the available AM surface area for Li⁺ to react and (de)intercalate. Indeed, the decrease in the active surface area upon calendering (Fig. 7C) is due to an increase in the AM-AM and AM-CBD contacts.

Within our model formality, the explicit consideration of CBD along the manufacturing and electrochemical simulations allowed a better understanding of the calendering role in structural mesoscopic observables (as the particles contacts evolution and the PSD), which can explain a macroscopic phenomenon (polarization). In this case, the electronic transport seems to be the limiting phenomenon in the simulated system: despite the decrease in the active surface area and the electrolyte transport efficiency, the polarization decreases through calendering for the case of the calendered electrodes.

The heterogeneities and mesoscopic properties discussed previously impact the Li intercalation in the NMC particles. Indeed, the size of the percolating network will drive the performance of the electrode at high C-rates, where a shift from a thermodynamically-driven system to a kinetically-driven one is observed [22]. Fig. 8 displays the 3D evolution of the NMC lithiation state at 110 mAh.g⁻¹ for the un-calendered and

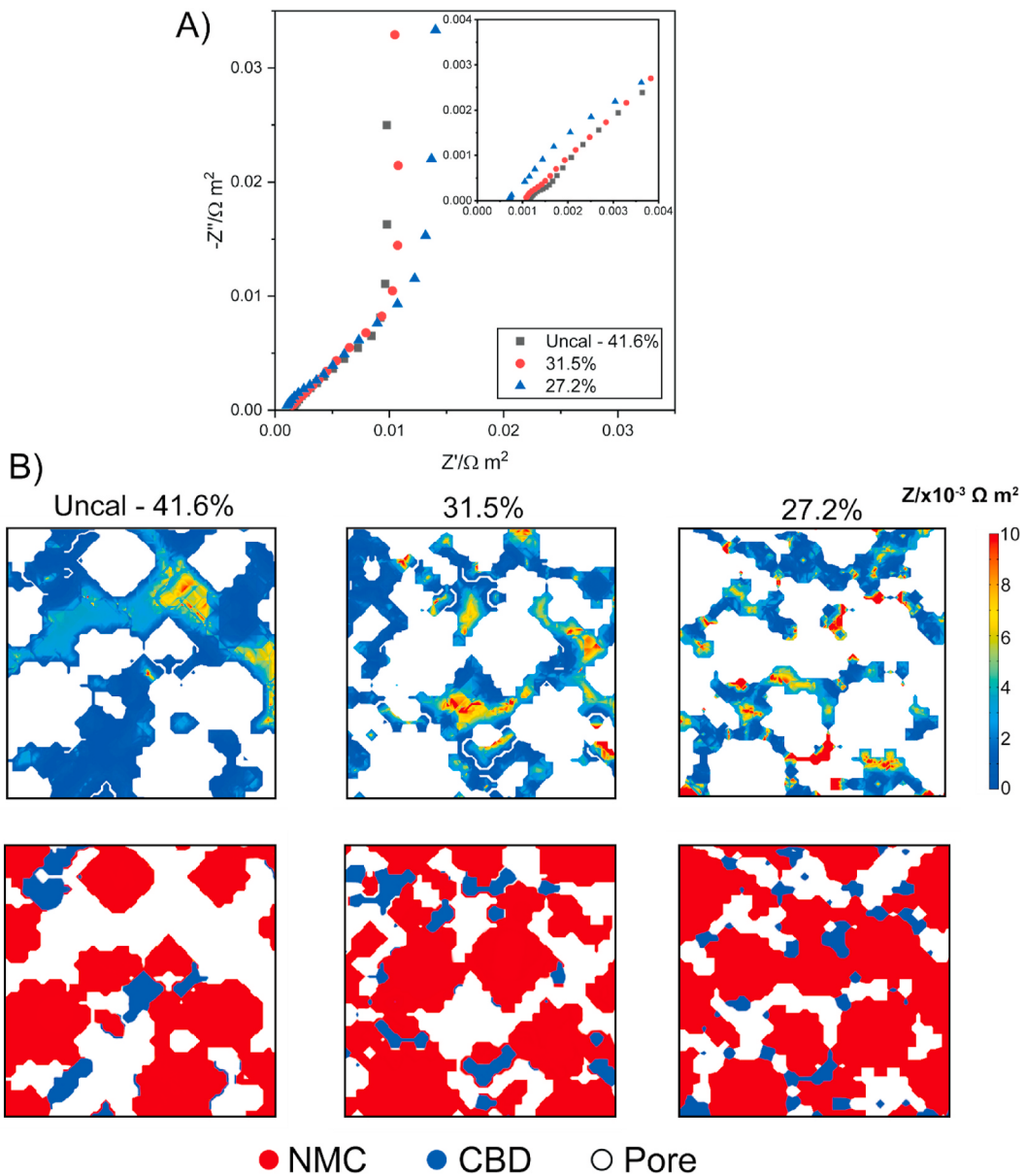


Fig. 6. (A) Simulated Nyquist plots for un-calendered and calendered electrodes in symmetric cell configuration. (B) (Top row) Electrode cross-sectional impedance 2D plots corresponding to the ionic contribution to the total measured impedance at half the electrode thickness at 100 Hz. (Bottom row) Scheme reporting the distribution of AM, CBDs and pore phases.

Table 3

Ionic resistances (R_{ion}) of the electrolyte within the porous electrode and associated tortuosity factors (τ_{EIS}) calculated according to the Transmission Line Model proposed by Landesfeind *et al.* [69].

| | $R_{ion} (\Omega \text{ m}^2)$ ^a | τ_{EIS} ^b |
|-------------|---|---------------------------|
| Uncal-41.6% | 0.02595 | 1.3676 |
| 31.5% | 0.02913 | 1.3808 |
| 27.2% | 0.04014 | 1.7527 |

^a Obtained from the graphical interpolation of the high-to-mid frequency region on the EIS spectra.

^b EIS-derived tortuosity obtained through the graphical method according to Landesfeind *et al.* [69].

calendered electrodes. On top of the clear difference in porosity, the difference in AM lithiation can also be observed. For each electrode, the region closer to the current collector has a higher lithiation state than the region closer to the separator, highlighting an electronic transport

limitation. In the un-calendered electrode there is a steeper gradient of concentration from top to bottom, *i.e.* a worse electronic conductivity, which is in agreement with the results reported in Fig. 7 (B,C). Also noteworthy, the lithiation state depends on the AM particle size distribution in the un-calendered and in the two calendered electrodes, even though the lithiation homogeneity is improved in the latter. The centers of the biggest AM particles remain less accessible to Li, whereas for smaller AM particles the degree of lithiation is almost complete. This implies that the particle size distribution is actually a predominant parameter for the electrode lithiation at high C-rate, because of the limiting solid Li diffusion through the AM. This contribution of the AM particle size distribution has already been evidenced in many experimental works [72–74].

5. Conclusions

In this work, we report the first experimentally validated 3D LIB electrode manufacturing digital twin considering both AM and CBD

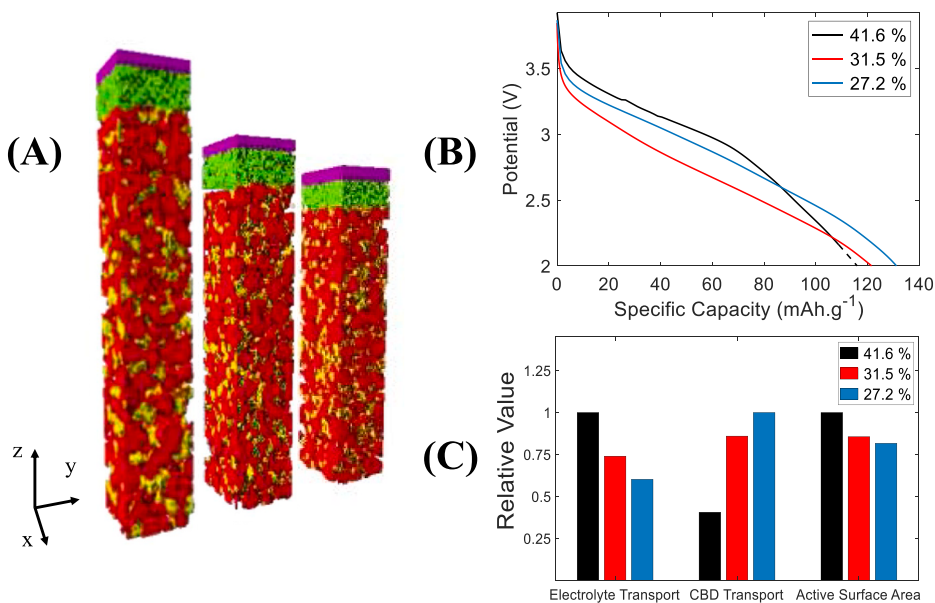


Fig. 7. (A) Meshed half-cells used for the electrochemical simulations (applied calendering pressure increases from left to right). In red, the AM; in yellow, the CBD; in green, the separator; and in purple, the Li foil. (B) Discharge curves as a function of the specific capacity (the dotted line is a fit to reach 2 V) for the un-calendered and calendered electrodes. (C) *Electrolyte Transport* (the inverse of the average Li^+ concentration gradient value along the z-axis); *CBD Transport* (defined as the inverse of the average standard deviation of local current density at the CBD surface); and the *Active Surface Area*, which refers to the AM surface area in contact with the electrolyte. (For interpretation of the references to colour in this figure legend, the reader is referred to the Web version of this article.)

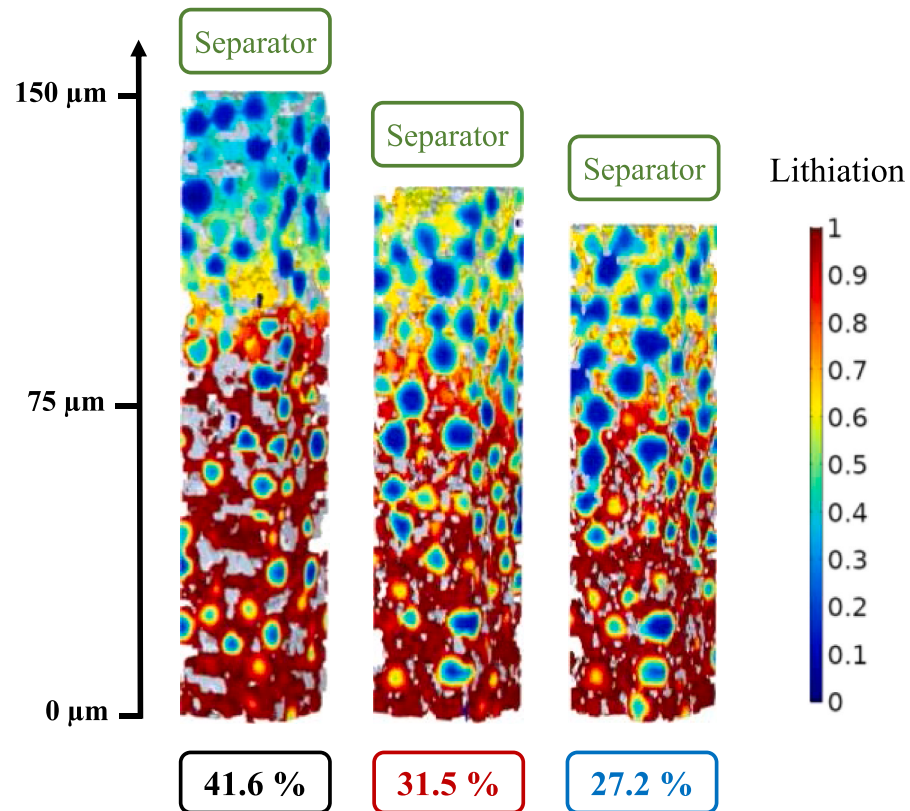


Fig. 8. Electrodes slices along the z axis for each condition showing their lithiation state ($[\text{Li}]_s/[\text{Li}]_{s,\text{max}}$) at the same discharge time, i.e. at 110 mAh.g^{-1} . The white phase stands for the electrolyte while the light grey one for the CBD.

phases for the case of $\text{LiNi}_{0.33}\text{Mn}_{0.33}\text{Co}_{0.33}\text{O}_2$ -based cathodes. This digital twin considers explicitly the slurry, dried and calendered electrode, whose associated properties were validated through comparison to *in house* experimental results. The latter was used to assess the effect of calendering on the mesostructural and electrochemical properties of cathodes containing 96 wt% of AM and 4 wt% of CBD. Specifically, the evolution of the PSD, tortuosity factor, particles arrangement, discharge galvanostatic performance and electrochemical impedance

spectroscopy were analyzed and discussed in detail.

In terms of the PSD both pores amount and dimensions decrease by increasing the calendering pressure, showing a good agreement with the experimental counterpart. The tortuosity factor increases by increasing the calendering pressure, as expected. The particles arrangement in the space was assessed through radial distribution function analysis. Particularly, it was observed that CBD particles tend to aggregate for both un-calendered and calendered electrodes. However, upon

calendering CBD aggregates are further compacted, which leads to a loss of order at longer distances (second shell) while increasing the AM particles coverage, thus filling the interstitial pores. In addition, it was observed that the calendering leads to a decrease in the AM-CBD distances. Nonetheless, above a certain calendering pressure, the AM-CBD distances cannot be further decreased. In terms of AM-AM radial distribution function, it was observed that a certain degree of local order was achieved through calendering. Lastly, the effect of calendering on the electrochemical properties of the electrode in terms of galvanostatic discharge and EIS was assessed. The results showed that for electrodes with low amount of carbon (as the one used herein) there is an increase of the discharge capacity at relatively high C-rate (1C) upon calendering (up to the maximal degree of calendering achieved along this work) due to the increased electronic conductivity of the electrode, while its ionic resistance and tortuosity factor increase. Moreover, the EIS spectra showed that the electronic and ionic resistance respectively decreases and increases upon calendering, as expected experimentally and in perfect accordance with the mesostructural analysis performed. The 4D performance simulations evidenced once more the capability of the sequential coupling between CGMD and DEM to model the electrode calendering.

The LIBs manufacturing digital twin presented in this article will be used in the near future by us to analyze the effect of the fabrication parameters on different electrode compositions and it will be further extended to consider other particles chemistries and shapes. Moreover, the calendering model here presented will be further completed in order to consider the primary NMC particles and the cracking of the secondary ones.

6. Methodology

6.1. Experimental section

$\text{LiNi}_{1/3}\text{Mn}_{1/3}\text{Co}_{1/3}\text{O}_2$ ($\rho = 4.653 \text{ g cm}^{-3}$, NMC) was supplied from Umicore. C-NERGYTM super C65 carbon black ($\rho = 1.834 \text{ g cm}^{-3}$, CB) was from IMERYS. SolefTM Polyvinylidene fluoride ($\rho = 1.791 \text{ g cm}^{-3}$, PVDF) was purchased from Solvay and N-methylpyrrolidone ($\rho = 1.028 \text{ g cm}^{-3}$, NMP) from BASF. The slurry solid components (NMC, CB and PVDF powders) were premixed with a soft blender. Afterwards, NMP was added until reaching 69% solid content. The total mass of solid components was around 65 g. The mixture was performed in a Dispemat CV3-PLUS high-shear mixer for 2 h in a water-bath cooled recipient at $25 \pm 1^\circ\text{C}$. The $\eta-\dot{\gamma}$ curves were acquired by applying a shear rate ramp (0.1–500 Hz) by using a rheometer (Kinexus lab+, Malvern Instruments), while the slurry density was measured through a density meter (DMA4500, Anton Paar GmbH). Both these properties were measured immediately after the slurry preparation.

The coating process was performed by a comma-gap machine (People & Technology Inc. model PDL-250) with a two built-in ovens, each one of 1 m long. The temperature of the two ovens were 80°C and 95°C , respectively. All the electrodes were coated over a 22 μm aluminum foil by fixing the comma gap and the line speed to 300 μm and 0.3 m min^{-1} , respectively. To calculate the electrode's porosity and density eight small circular disks of 13 mm of diameter were punched, and their mass and thickness measured, in different zones of the coated aluminum.

The calendering was performed through a prototype-grade lap press calender (BPN250, People & Technology, Korea), consisting in a two-roll compactor of 25 cm of diameter in which the gap between the rolls controls the pressure applied to the electrodes. The roll gaps were converted into applied pressure by using force sensor films (ELF measuring system equipped with FlexiForce sensors, Tekscan). Furthermore, both the roll speed and the roll temperature can be controlled. The calendering was performed at various applied pressures and at constant line speed (0.54 m min^{-1}) and roll temperature (60°C).

Micro-indentation experiments were carried out at room

temperature with a microhardness Tester (MHT, CSM Instruments) equipped with a Vickers diamond indenter. The loading/unloading rate was 0.4 mN s^{-1} and the maximum load for all the indentation experiments was of 200 mN, which ensures an indenter penetration lower than 10% of the electrodes thickness, in order to avoid substrate effects. The indenter was maintained at the maximum load during 3 s. Thirty indentation tests were performed to ensure representative results.

6.2. Computational Methods

The CGMD simulations were performed in an NPT environment at 298 K and 1 atm, while the DEM simulations were performed in an NVE environment where the pressure was controlled by the moving plane in order to mimic the calender rolls. All the details about the initial structure generation can be found in the Supporting information (Section S2) of Ref. [18]. The density of compact CBD particles (without consideration of the nanoporosity, i.e. 1.81 g cm^{-3}) was calculated by the average of the experimental density of carbon black and PVDF. The CGMD simulations were performed by using periodic boundary conditions on x, y and z through the open source computational software LAMMPS [75]. The slurry and dried electrode simulations (396 AM particles and 9463 CBD particles) took respectively ~ 5 and ~ 33 h by using one node (128 GB of RAM) composed of 2 processors (Intel® Xeon® CPU E5-2680 v4 @ 2.40 GHz, 14 cores) on the MatriCs platform (Université de Picardie-Jules Verne). The initial structure (prior the slurry equilibration) was generated to match the experimental composition and AM particles size distribution by locating randomly the AM and CBD particles in a simulation box big enough ($200 \times 200 \times 1200 \mu\text{m}$, $x \times y \times z$) in order to avoid particles overlap. All the details about the random structure generation can be found in the Supporting Information of Ref. [18]. The slurry and dried electrode density were calculated dividing the total mass of the particles by the simulation box volume at the end of the simulation.

The DEM simulations were carried out by using the open source computational software LIGGGHTS [76]. The timestep used for the calendering simulation is equal to 0.1 ns, while the number of timesteps varied between 13×10^7 and 20×10^7 (as a function of the level of compression desired) by moving the upper plane at a speed of 0.002 m s^{-1} . The same number of timesteps and speed (but in the opposite direction) was used for the decompression step. The plane speed was selected in order to minimize the computational cost and maximize the numerical stability of the simulations. Several tests were performed to verify the effect of lowering the plane speed, showing that its effect is negligible, as discussed in the Supporting Information, Section S6. The planes were initially located at a distance of few micrometers respect the limit of the CGMD structure to avoid overlapping between the planes and the particles. The applied calendered pressure was calculated as the force applied at the electrode upper plane at the maximal compression, divided by its surface. Concerning the computational cost, by using the pristine dried electrode structure, the calendering simulations took between 20 and 40 h as a function of the level of compression desired and by employing the same computational resources of the CGMD simulations. In order to consider a bigger surface area along the indentation measurements the pristine electrode were replicated four times along both at x and y directions ($\sim 160,000$ particles). The same speed and timestep as the calendering simulation were used. However, the number of the timesteps were $8 \times 10^7/8 \times 10^7$ for the compression/decompression steps, in order to reach a compression of $\sim 10\%$ the initial electrode thickness, as discussed above. The latter simulation took approximately 4 days by using two nodes (128 GB of RAM) composed of 2 processors each (Intel® Xeon® CPU E5-2680 v4 @ 2.40 GHz, 14 cores) on the MatriCs platform (Université de Picardie-Jules Verne).

The open-source PorosityPlus algorithm [57] was used to calculate the electrodes (calendered and not) porosity and the PSD without considering the 2% particle expansions implemented in the GH FF, as discussed in Section 2. The calendered electrodes height (needed for the

PorosityPlus code) was measured as the highest point of the upper plane (during the decompression) in which a contact $\neq 0$ between the upper plane and the electrode was computed. Moreover, in accordance to the boundary conditions of the DEM simulation, the x and y directions were considered as periodic for the pore size distribution calculation, while z was considered as not periodic. For the PSD analyses of the un-calendered electrode, all the directions were considered as periodic (as in the case of the CGMD simulations).

The calculation of the tortuosity factors in the three Cartesian directions x , y , and z , was done with the GeoDict [65] software package. The structures generated from CGMD/DEM simulations were first converted to grayscale .tiff image files with a $0.25\text{ }\mu\text{m}$ voxel size. Then, ImportGeo-Vol package was used to import the images into native .gdt files, by properly thresholding them in order to obtain well-differentiated pore, AM, and CBD phases. Lastly, the DiffuDict package was used to simulate the diffusion experiment, by assigning effective diffusivities to the pore ($7.5 \times 10^{-11}\text{ m}^2\text{ s}^{-1}$) and CBD ($2.46 \times 10^{-11}\text{ m}^2\text{ s}^{-1}$) phases, as explained in Section 3.

The un-calendered and calendered CGMD/DEM structures were meshed using the *in house* algorithm INNOV, fully explained in our previous article [67]. In short, from the coordinates of the particles centers, 2D slices were generated while keeping the periodic boundary conditions. Then, a $12\text{ }\mu\text{m}$ Celgard separator (coming from a SEM image of $13 \times 7 \times 5\text{ }\mu\text{m}^3$) [68] was added. To fit the dimensions of the electrodes, it was duplicated in every direction and cropped to ensure the desired dimensions. On top of this separator, a $5\text{ }\mu\text{m}$ thick homogeneous Li foil negative electrode was added. Finally, these slices were fed into the INNOV voxelization-based code to generate the multiphase volumetric mesh. The electrodes dimensions were $25.8 \times 25.8 \times z\text{ }\mu\text{m}^3$, with z equal to $165.0, 141.6, 133.8\text{ }\mu\text{m}$ with increasing calendering pressure. Each mesh is composed of more than 800 000 elements.

Once imported into COMSOL Multiphysics®, an electrochemical model was applied to simulate a single discharge at 1C starting from a fully charged battery. The model is identical to the one reported in our previous study [20], except for the AM electronic conductivity, which was decreased down to $5 \times 10^{-3}\text{ S m}^{-1}$, similarly to values found experimentally [77]. The CBD was treated as partially open, meaning the transport of Li^+ within that phase was allowed with an effective diffusion coefficient and no intercalation at the CBD-electrolyte interface was permitted. All CBD effective transport properties were corrected with the Bruggeman relation taking into account an inner porosity of 47%. The Li solid diffusion coefficient within the NMC was fixed at $2 \times 10^{-15}\text{ m}^2\text{ s}^{-1}$. The discharge simulations took between 5 and 9 h on a laboratory server with 256 GB of RAM.

The EIS tests were also performed in COMSOL Multiphysics environment. The Batteries & Fuel Cells and the Transport of Diluted species modules were implemented for the calculations. The impedance was measured at seven frequencies per decade, ranging from 1 to 10^7 Hz and applying a 10 mV sinusoidal perturbation. All the cell parameters and constants used for the EIS simulations are listed in our recent publication [21]. To keep the consistency between discharge and EIS simulations, input parameter such as porosity of CBD was adapted to the ones of the discharge simulations. In addition, AM's electronic conductivity was assumed equal to 1 S m^{-1} to neglect the role of electronic resistance [69]. The tests were performed using an Intel® Xeon® E5-4627 Cache @ 3.30 GHz with 264 GB of RAM. Each simulation took between 24 and 36 h, depending on the electrode structure. For calculating τ_{EIS} , the effective electrolyte ionic conductivity was derived from the Nyquist plot, according to Landesfeind et al. [69]. Briefly, the observed response can be fitted with a transmission line model (TLM) in series with a high frequency resistance (corresponding to the separator resistance + electrode resistance). The TLM accounts for the resistance of the ionic path (*i.e.* ions within the pores) at mid-to-high frequencies, while the low frequency capacitive behavior corresponds the double layer formation. R_{ion} can be graphically extracted, by multiplying by 3 the real axis projection of the sloping mid-to-high frequency part. Further

information can be found in Ref. [21].

CRediT authorship contribution statement

Alain C. Ngandjou: Conceptualization, Methodology, Software, Validation, Formal analysis, Investigation, Visualization. **Teo Lombardo:** Conceptualization, Methodology, Software, Validation, Formal analysis, Investigation, Writing - original draft, Writing - review & editing, Visualization. **Emiliano N. Primo:** Conceptualization, Formal analysis, Investigation, Writing - review & editing, Visualization. **Mehdi Chouchane:** Conceptualization, Methodology, Software, Formal analysis, Investigation, Writing - review & editing, Visualization. **Abbos Shodiev:** Conceptualization, Methodology, Software, Formal analysis, Investigation, Writing - review & editing, Visualization. **Oier Arcelus:** Software, Formal analysis, Investigation, Writing - review & editing. **Alejandro A. Franco:** Conceptualization, Methodology, Writing - review & editing, Supervision, Project administration, Funding acquisition.

Declaration of competing interest

The authors declare that they have no known competing financial interests or personal relationships that could have appeared to influence the work reported in this paper.

Acknowledgements

The authors acknowledge the European Union's Horizon 2020 research and innovation programme for the funding support through the European Research Council (grant agreement 772873, "ARTISTIC" project). A.A.F. acknowledges Institut Universitaire de France for the support. CGMD and DEM results were achieved thanks to the Matrics HPC platform from Université de Picardie-Jules Verne, particularly using the ARTISTIC project-dedicated computational nodes. The authors acknowledge Dr. Garima Shukla from LRCS-Amiens (France) for providing the experimental manufacturing scheme used as baseline for the graphical abstract.

Appendix A. Supplementary data

Supplementary data to this article can be found online at <https://doi.org/10.1016/j.jpowsour.2020.229320>.

Appendix B. Data and code availability

All the codes used along this work are going to be published in the computational portal of the ARTISTIC website [78] and in its associated GitHub page (<https://github.com/ARTISTIC-ERC/Manufacturing-Model-Codes>).

References

- [1] A. Opitz, P. Badami, L. Shen, K. Vignarooban, A.M. Kannan, Can Li-Ion batteries be the panacea for automotive applications? *Renew. Sustain. Energy Rev.* 68 (1) (2017) 685–692, <https://doi.org/10.1016/j.rser.2016.10.019>.
- [2] G. Zubi, R. Dufó-López, M. Carvalho, G. Pasaoğlu, The lithium-ion battery: state of the art and future perspectives, *Renew. Sustain. Energy Rev.* 89 (2018) 292–308, <https://doi.org/10.1016/j.rser.2018.03.002>.
- [3] B. Dunn, H. Kamath, J.M. Tarascon, Electrical energy storage for the grid: a battery of choices, *Science* 30 (2011) 928–935, <https://doi.org/10.1126/science.1212741>, 334.
- [4] D. J.-M.T. Larcher, Towards greener and more sustainable batteries for electrical energy storage, *Nat. Chem.* 7 (2015) 19–29, <https://doi.org/10.1038/NCHEM.2085>.
- [5] N. Nitta, F. Wu, J.T. Lee, G. Yushin, Li-ion battery materials: present and future, *Mater. Today* 18 (2015) 252–264, <https://doi.org/10.1016/j.mattod.2014.10.040>.
- [6] J.F. Peters, M. Baumann, B. Zimmermann, J. Braun, M. Weil, The environmental impact of Li-Ion batteries and the role of key parameters – a review, *Renew. Sustain. Energy Rev.* 67 (2017) 491–506, <https://doi.org/10.1016/j.rser.2016.08.039>.

- [7] G.E. Blomgren, The development and future of lithium ion batteries, *J. Electrochem. Soc.* 164 (2017) A5019–A5025, <https://doi.org/10.1149/2.0251701jes>.
- [8] D.L. Wood, J. Li, C. Daniel, Prospects for reducing the processing cost of lithium ion batteries, *J. Power Sources* 275 (2015) 234–242, <https://doi.org/10.1016/j.jpowsour.2014.11.019>.
- [9] M. Thomitzek, O. Schmidt, F. Röder, U. Krewer, C. Herrmann, S. Thiede, Simulating process-product interdependencies in battery production systems, *Procedia CIRP* 72 (2018) 346–351, <https://doi.org/10.1016/j.procir.2018.03.056>.
- [10] A. Turetkyy, S. Thiede, M. Thomitzek, N. von Drachenfels, T. Pape, C. Herrmann, Toward data-driven applications in lithium-ion battery cell manufacturing, *Energy Technol.* (2019) 1900136, <https://doi.org/10.1002/ente.201900136>, 1900136.
- [11] L.S. Kremer, A. Hoffmann, T. Danner, S. Hein, B. Prifling, D. Westhoff, C. Dreer, A. Latz, V. Schmidt, M. Wohlfahrt-Mehrens, Manufacturing process for improved ultra-thick cathodes in high-energy lithium-ion batteries, *Energy Technol.* 8 (2020), <https://doi.org/10.1002/ente.201900167>.
- [12] S. Jaiser, M. Müller, M. Baunach, W. Bauer, P. Schärfer, W. Schabel, Investigation of film solidification and binder migration during drying of Li-Ion battery anodes, *J. Power Sources* 318 (2016) 210–219, <https://doi.org/10.1016/j.jpowsour.2016.04.018>.
- [13] J.K. Mayer, L. Almar, E. Asylbekov, W. Haselrieder, A. Kwade, A. Weber, H. Nirschl, Influence of the carbon black dispersing process on the microstructure and performance of Li-ion battery cathodes, *Energy Technol.* 8 (2020) 1900161, <https://doi.org/10.1002/ente.201900161>.
- [14] W. Bauer, D. Nötzel, V. Wenzel, H. Nirschl, Influence of dry mixing and distribution of conductive additives in cathodes for lithium ion batteries, *J. Power Sources* 288 (2015) 359–367, <https://doi.org/10.1016/j.jpowsour.2015.04.081>.
- [15] H. Bockholt, W. Haselrieder, A. Kwade, Intensive powder mixing for dry dispersing of carbon black and its relevance for lithium-ion battery cathodes, *Powder Technol.* 297 (2016) 266–274, <https://doi.org/10.1016/j.powtec.2016.04.011>.
- [16] T.-J. Liu, C. Tiu, L.-C. Chen, D. Liu, The influence of slurry rheology on lithium-ion electrode processing, in: S. Lanceros-Méndez, C.M. Costa (Eds.), *Print. Batter. John Wiley & Sons Ltd.*, 2018, pp. 63–79, <https://doi.org/10.1002/9781119287902.ch3>.
- [17] A.A. Franco, A. Rucci, D. Brandell, C. Frayret, M. Gaberscek, P. Jankowski, P. Johansson, Boosting rechargeable batteries R&D by multiscale modeling: myth or reality? *Chem. Rev.* 119 (2019) 4569–4627, <https://doi.org/10.1021/acs.chemrev.8b00239>.
- [18] T. Lombardo, J. Hoock, E.N. Primo, A.C. Ngandjou, M. Duquesnoy, A.A. Franco, Accelerated optimization methods for force-field parametrization in battery electrode manufacturing modeling, *Batter. Supercaps.* 3 (2020) 1–11, <https://doi.org/10.1002/batt.202000049>.
- [19] I. Srivastava, D.S. Bolintineanu, J.B. Lechman, A. Scott, Controlling binder adhesion to impact electrode mesostructure and transport, *ACS Appl. Mater. Interfaces* (2020), <https://doi.org/10.1149/osf.io/ehdq6>.
- [20] M. Chouchane, E.N. Primo, A.A. Franco, Mesoscale effects in the extraction of the solid-state lithium diffusion coefficient values of battery active materials: physical insights from 3D modeling, *J. Phys. Chem. Lett.* (2020) 2775–2780, <https://doi.org/10.1021/acs.jpclett.0c00517>.
- [21] A. Shodiev, E.N. Primo, M. Chouchane, T. Lombardo, A.C. Ngandjou, A. Rucci, A. A. Franco, 4D-resolved physical model for Electrochemical Impedance Spectroscopy of Li(Ni_{1-x}yMnxCoy)O₂-based cathodes in symmetric cells: consequences in tortuosity calculations, *J. Power Sources* 444 (2020) 227871, <https://doi.org/10.1016/j.jpowsour.2020.227871>.
- [22] M. Chouchane, A. Rucci, T. Lombardo, A.C. Ngandjou, A.A. Franco, Lithium ion battery electrodes predicted from manufacturing simulations : assessing the impact of the carbon-binder spatial location on the electrochemical performance, *J. Power Sources* 444 (2019) 227285, <https://doi.org/10.1016/j.jpowsour.2019.227285>.
- [23] A. Rucci, A.C. Ngandjou, E.N. Primo, M. Maiza, A.A. Franco, Tracking variabilities in the simulation of Lithium Ion Battery electrode fabrication and its impact on electrochemical performance, *Electrochim. Acta* (2019), <https://doi.org/10.1016/j.electacta.2019.04.110>.
- [24] A.C. Ngandjou, A. Rucci, M. Maiza, G. Shukla, J. Vazquez-Arenas, A.A. Franco, Multiscale simulation platform linking lithium ion battery electrode fabrication process with performance at the cell level, *J. Phys. Chem. Lett.* 8 (2017) 5966–5972, <https://doi.org/10.1021/acs.jpclett.7b02647>.
- [25] M.E. Ferraro, B.L. Trembacki, V.E. Brunini, D.R. Noble, S.A. Roberts, Electrode mesoscale as a collection of particles: coupled electrochemical and mechanical analysis of NMC cathodes, *J. Electrochem. Soc.* 167 (2020), 013543, <https://doi.org/10.1149/1945-7111/ab632b>.
- [26] X. Lu, A. Bertei, D.P. Finegan, C. Tan, S.R. Daemi, J.S. Weaving, K.B.O. Regan, T.M. M. Heenan, G. Hinds, E. Kendrick, D.J.L. Brett, P.R. Shearing, 3D microstructure design of lithium-ion battery electrodes assisted by X-ray nano-computed tomography and modelling, *Nat. Commun.* 11 (2020) 1–13, <https://doi.org/10.1038/s41467-020-15811-x>.
- [27] M.M. Forouzan, C.W. Chao, D. Bustamante, B.A. Mazzeo, D.R. Wheeler, Experiment and simulation of the fabrication process of lithium-ion battery cathodes for determining microstructure and mechanical properties, *J. Power Sources* 312 (2016) 172–183, <https://doi.org/10.1016/j.jpowsour.2016.02.014>.
- [28] B.L. Trembacki, D.R. Noble, V.E. Brunini, M.E. Ferraro, S.A. Roberts, Mesoscale effective property simulations incorporating conductive binder, *J. Electrochem. Soc.* 164 (2017) E3613–E3626, <https://doi.org/10.1149/2.0601711jes>.
- [29] T. Danner, M. Singh, S. Hein, J. Kaiser, H. Hahn, A. Latz, Thick electrodes for Li-ion batteries: a model based analysis, *J. Power Sources* 334 (2016) 191–201, <https://doi.org/10.1016/j.jpowsour.2016.09.143>.
- [30] M. Ebner, F. Geldmacher, F. Marone, M. Stampanoni, V. Wood, X-ray tomography of porous, transition metal oxide based lithium ion battery electrodes, *Adv. Energy Mater.* 3 (2013) 845–850, <https://doi.org/10.1002/aenm.201200932>.
- [31] P. Pietsch, V. Wood, X-ray tomography for lithium ion battery research: a practical guide, *Annu. Rev. Mater. Res.* 47 (2017) 451–479, <https://doi.org/10.1146/annurev-matsci-070616-123957>.
- [32] P. Pietsch, M. Ebner, F. Marone, M. Stampanoni, V. Wood, Determining the uncertainty in microstructural parameters extracted from tomographic data, *Sustain. Energy Fuels* 2 (2018) 598–605, <https://doi.org/10.1039/c7se00498b>.
- [33] H. Zheng, L. Tan, G. Liu, X. Song, V.S. Battaglia, Calendering effects on the physical and electrochemical properties of Li[Ni 1/3Mn 1/3Co 1/3]O 2 cathode, *J. Power Sources* 208 (2012) 52–57, <https://doi.org/10.1016/j.jpowsour.2012.02.001>.
- [34] C. Meyer, H. Bockholt, W. Haselrieder, A. Kwade, Characterization of the calendering process for compaction of electrodes for lithium-ion batteries, *J. Mater. Process. Technol.* 249 (2017) 172–178, <https://doi.org/10.1016/j.jmatprotec.2017.05.031>.
- [35] C. Meyer, M. Weyhe, W. Haselrieder, A. Kwade, Heated calendering of cathodes for lithium-ion batteries with varied carbon black and binder contents, *Energy Technol.* 8 (2020) 1900175, <https://doi.org/10.1002/ente.201900175>.
- [36] A. van Bommel, R. Divigalpitiya, Effect of calendering LiFePO₄ electrodes, *J. Electrochem. Soc.* 159 (2012) A1791–A1795, <https://doi.org/10.1149/2.029211jes>.
- [37] C. Meyer, M. Kosfeld, W. Haselrieder, A. Kwade, Process modeling of the electrode calendering of lithium-ion batteries regarding variation of cathode active materials and mass loadings, *J. Energy Storage* 18 (2018) 371–379, <https://doi.org/10.1016/j.est.2018.05.018>.
- [38] D. Schreiner, M. Oguntke, T. Günther, G. Reinhart, Modelling of the calendering process of NMC-622 cathodes in battery production analyzing machine/material-process-structure correlations, *Energy Technol.* 7 (2019) 1900840, <https://doi.org/10.1002/ente.201900840>.
- [39] C. Sangrós Giménez, C. Schilde, L. Froböse, S. Ivanov, A. Kwade, Mechanical, electrical, and ionic behavior of lithium-ion battery electrodes via discrete element method simulations, *Energy Technol.* (2019), <https://doi.org/10.1002/ente.201900180>.
- [40] C. Sangrós Giménez, B. Finke, C. Nowak, C. Schilde, A. Kwade, Structural and mechanical characterization of lithium-ion battery electrodes via DEM simulations, *Adv. Powder Technol.* 29 (2018) 2312–2321, <https://doi.org/10.1016/j.ap.2018.05.014>.
- [41] C. Sangrós Giménez, B. Finke, C. Schilde, L. Froböse, A. Kwade, Numerical simulation of the behavior of lithium-ion battery electrodes during the calendering process via the discrete element method, *Powder Technol.* 349 (2019) 1–11, <https://doi.org/10.1016/j.powtec.2019.03.020>.
- [42] A.J. Stershic, S. Simunovic, J. Nanda, Modeling the evolution of lithium-ion particle contact distributions using a fabric tensor approach, *J. Power Sources* 297 (2015) 540–550, <https://doi.org/10.1016/j.jpowsour.2015.07.088>.
- [43] S.G. Lee, D.H. Jeon, Effect of electrode compression on the wettability of lithium-ion batteries, *J. Power Sources* 265 (2014) 363–369, <https://doi.org/10.1016/j.jpowsour.2014.04.127>.
- [44] M. Duquesnoy, T. Lombardo, M. Chouchane, E.N. Primo, A. Alejandro, Accelerating battery manufacturing optimization by combining experiments, in: *Silico Electrodes Generation and Machine Learning*, *ChemRxiv*. Prepr. vols. 1–33, 2020, [https://doi.org/10.1002/aenm.201401612](https://doi.org/10.26434/chemrxiv.12473501.v.</p>
<p>[45] L. Ziecke, T. Hutzenthaler, D.R. Wheeler, C.W. Chao, I. Manke, A. Hilger, N. Paust, R. Zengerle, S. Thiele, Three-phase multiscale modeling of a LiCoO₂ cathode: combining the advantages of FIB-SEM imaging and X-ray tomography, <i>Adv. Energy Mater.</i> 5 (2015) 1–8, <a href=).
- [46] https://lammps.sandia.gov/doc/pair_lj.html (n.d.).
- [47] https://lammps.sandia.gov/doc/pair_gran.html#pair-style-gran-hertz-history-command (n.d.).
- [48] https://www.cfdem.com/media/DEM/doc/gran_model_hertz.html (n.d.).
- [49] D.K. Davies, Surface charge and the contact of elastic solids, *J. Phys. D Appl. Phys.* 6 (1973) 1017–1024, <https://doi.org/10.1088/0022-3727/6/9/304>.
- [50] https://www.cfdem.com/media/DEM/doc/gran_cohesion_sjkr.html (n.d.).
- [51] https://lammps.sandia.gov/doc/pair_gran.html (n.d.).
- [52] https://www.engineeringtoolbox.com/young-modulus-d_417.html (n.d.).
- [53] R. Xu, H. Sun, L.S. de Vasconcelos, K. Zhao, Mechanical and structural degradation of LiNi_x Mn_y Co_z O₂ cathode in Li-ion batteries: an experimental study, *J. Electrochem. Soc.* 164 (2017) A3333–A3341, <https://doi.org/10.1149/2.1751713jes>.
- [54] L.S. de Vasconcelos, R. Xu, J. Li, K. Zhao, Grid indentation analysis of mechanical properties of composite electrodes in Li-ion batteries, *Extrem. Mech. Lett.* 9 (2016) 495–502, <https://doi.org/10.1016/j.eml.2016.03.002>.
- [55] E.J. Cheng, K. Hong, N.J. Taylor, H. Choe, J. Wolfenstine, J. Sakamoto, Mechanical and physical properties of LiNi_{0.33}Mn_{0.33}Co_{0.33}O₂ (NMC), *J. Eur. Ceram. Soc.* 37 (2017) 3213–3217, <https://doi.org/10.1016/j.jeurceramsoc.2017.03.048>.
- [56] G. Constantinides, K.S. Ravi Chandran, F.-J. Ulm, K.J. Van Vliet, Grid indentation analysis of composite microstructure and mechanics: principles and validation, *Mater. Sci. Eng.* 430 (2006) 189–202, <https://doi.org/10.1016/j.msea.2006.05.125>.
- [57] <https://research.csiro.au/mmm/porosityplus/> (n.d.).
- [58] G. Opletal, T.C. Petersen, I.K. Snook, D.G. McCulloch, Modeling of structure and porosity in amorphous silicon systems using Monte Carlo methods, *J. Chem. Phys.* 126 (2007), <https://doi.org/10.1063/1.2743029>.
- [59] S. Amziane (Ed.), *Bio-aggregates Based Building Materials State-Of-The-Art Report of the RILEM Technical Committee - Chapter 2*, Springer, 2017, https://doi.org/10.1007/978-94-024-1031-0_2.

- [60] E.W. Washburn, The dynamics of capillary flow, *Phys. Rev.* 17 (1921) 273–283.
- [61] H. Dong, M.J. Blunt, Pore-network extraction from micro-computerized-tomography images, *Phys. Rev. E - Stat. Nonlinear Soft Matter Phys.* 80 (2009) 1–11, <https://doi.org/10.1103/PhysRevE.80.036307>.
- [62] A. Torayev, A. Rucci, P.C.M.M. Magusin, A. Demortière, V. De Andrade, C.P. Grey, C. Merlet, A.A. Franco, Stochasticity of pores interconnectivity in Li-O₂ batteries and its impact on the variations in electrochemical performance, *J. Phys. Chem. Lett.* 9 (2018) 791–797, <https://doi.org/10.1021/acs.jpclett.7b03315>.
- [63] B. Tjaden, D.J.L. Brett, P.R. Shearing, Tortuosity in electrochemical devices: a review of calculation approaches, *Int. Mater. Rev.* 63 (2018) 47–67, <https://doi.org/10.1080/09506608.2016.1249995>.
- [64] R.B. MacMullin, G.A. Muccini, Characteristics of porous beds and structures, *AIChE J.* 2 (1956) 393–403, <https://doi.org/10.1002/aic.690020320>.
- [65] <https://www.math2market.com/> (n.d.).
- [66] N. Epstein, On tortuosity and the tortuosity factor in flow and diffusion through porous media, *Chem. Eng. Sci.* 44 (1989) 777–779, [https://doi.org/10.1016/0009-2509\(89\)85053-5](https://doi.org/10.1016/0009-2509(89)85053-5).
- [67] M. Chouchane, A. Rucci, A.A. Franco, A versatile and efficient voxelization-based meshing algorithm of multiple phases, *ACS Omega* 4 (2019) 11141–11144, <https://doi.org/10.1021/acsomega.9b01279>.
- [68] M.F. Lagadec, V. Wood, Microstructure of Celgard® PP1615 Lithium-Ion Battery Separator, 2018.
- [69] J. Landesfeind, J. Hattendorff, A. Ehrl, W.A. Wall, H.A. Gasteiger, Tortuosity determination of battery electrodes and separators by impedance spectroscopy, *J. Electrochem. Soc.* 163 (2016) A1373–A1387, <https://doi.org/10.1149/2.1141607jes>.
- [70] S. Malifarge, B. Delobel, C. Delacourt, Determination of tortuosity using impedance spectra analysis of symmetric cell, *J. Electrochem. Soc.* 164 (2017) E3329–E3334, <https://doi.org/10.1149/2.0331711jes>.
- [71] J. Landesfeind, A. Eldiven, H.A. Gasteiger, Influence of the binder on lithium ion battery electrode tortuosity and performance, *J. Electrochem. Soc.* 165 (2018) A1122–A1128, <https://doi.org/10.1149/2.0971805jes>.
- [72] N.N. Sinha, N. Munichandraiah, The effect of particle size on performance of cathode materials of Li-ion batteries, *J. Indian Inst. Sci.* 89 (2009) 381–392.
- [73] C.-C. Chang, J.Y. Kim, P.N. Kumta, Influence of crystallite size on the electrochemical properties of chemically synthesized stoichiometric LiNiO₂[sub 2], *J. Electrochem. Soc.* 149 (2002) A1114, <https://doi.org/10.1149/1.1495495>.
- [74] S.W. Lee, S.G. Lee, K.S. Han, Sub-micron LiCoO₂ manufactured in a single synthetic step using eutectic self-mixing method, *J. Power Sources* 163 (2006) 274–277, <https://doi.org/10.1016/j.jpowsour.2006.05.041>.
- [75] <https://lammps.sandia.gov/>, (n.d.). <https://doi.org/1>.
- [76] <https://www.cfdem.com/liggghts-open-source-discrete-element-method-particle-simulation-code> (n.d.).
- [77] Y.-H. Chen, C.-W. Wang, G. Liu, X.-Y. Song, V.S. Battaglia, A.M. Sastry, Selection of conductive additives in Li-ion battery cathodes, *J. Electrochem. Soc.* 154 (2007) A978, <https://doi.org/10.1149/1.2767839>.
- [78] <https://www.u-picardie.fr/erc-artistic/computational-portal/> (n.d.).